Segmentation of Loops from Coronal EUV Images

B. Inhester · L. Feng · T. Wiegelmann

Abstract We present a procedure to extract bright loop features from solar EUV images. In terms of image intensities, these features are elongated ridge-like intensity maxima. To discriminate the maxima, we need information about the spatial derivatives of the image intensity. Commonly, the derivative estimates are strongly affected by image noise. We therefore use a regularized estimation of the derivative, which is then used to interpolate a discrete vector field of ridge points; these "ridgels" are positioned on the ridge center and have the intrinsic orientation of the local ridge direction. A scheme is proposed to connect ridgels to smooth, spline-represented curves that fit the observed loops. Finally, a half-automated user interface allows one to merge or split curves or eliminate or select loop fits obtained from this procedure. In this paper we apply our tool to one of the first EUV images observed by the SECCHI instrument onboard the recently launched STEREO spacecraft. We compare the extracted loops with projected field lines computed from near-simultaneous magnetograms measured by the SOHO/MDI Doppler imager. The field lines were calculated by using a linear force-free field model. This comparison allows one to verify faint and spurious loop connections produced by our segmentation tool and it also helps to prove the quality of the magnetic-field model where well-identified loop structures comply with field-line projections. We also discuss further potential applications of our tool such as loop oscillations and stereoscopy.

Keywords EUV images · Coronal magnetic fields · Image processing

1. Introduction

Solar EUV images offer a wealth of information about the structure of the solar chromosphere, transition region, and corona. Moreover, these structures are in continuous mo-

B. Inhester (✉) · L. Feng · T. Wiegelmann
Max-Planck-Institut für Sonnensystemforschung, Max-Planck-Str. 2, 37191 Katlenburg-Lindau, Germany
e-mail: inhester@mps.mpg.de

L. Feng
Purple Mountain Observatory, Chinese Academy of Sciences, Nanjing, China

tion so that the information collected by EUV images of the Sun is enormous. For many purposes this information must be reduced. A standard task for many applications (*e.g.*, for the comparison with projected field lines computed from a coronal magnetic-field model or for tie-point stereoscopic reconstruction) requires the extraction of the shape of bright loops from these images.

Solar physics shares this task of ridge detection with many other disciplines in physics and also in other areas of research. A wealth of different approaches for the detection and segmentation of ridges has been proposed ranging from multiscale filtering (Koller *et al.*, 1995; Lindeberg, 1998) and curvelet and ridgelet transforms (Starck, Donoho, and Candès, 2003) to snake and watershed algorithms (Nguyen, Worring, and van den Boomgaard, 2000) and combining detected ridge points by tensor voting (Medioni, Tang, and Lee, 2000). These general methods however always need to be modified and optimized for specific applications. Much work in this field has been motivated by medical imaging (*e.g.*, Jang and Hong, 2002; Dimas, Scholz, and Obermayer, 2002) and also by the application in more technical fields such as fingerprint classification (Zhang and Yan, 2004) and the detection of roads in areal photography (Steger, 1998).

For the automated segmentation of loops, a first step was made by Strous (2002, unpublished) who proposed a procedure to detect pixels in the vicinity of loops. This approach was further extended by Lee, Newman, and Gary (2006) by means of a connection scheme that makes use of a local solar-surface magnetic-field estimate to obtain a preferable connection orientation. The procedure then leads to spline curves as approximations for the loop shapes in the image. The method gave quite promising results for artificial and also for observed trace EUV images.

The program presented here can be considered an extension of the work by Lee, Newman, and Gary (2006). The improvements we propose are to replace Strous's ridge-point detection scheme by a modified multiscale approach of Lindeberg (1998), which automatically adjusts to varying loop thicknesses and also returns an estimate of the reliability of the ridge point location and orientation. When connecting the ridge points, we would prefer not to use any magnetic-field information as this prejudices a later comparison of the extracted loops with field lines computed from an extrapolation of the surface magnetic field. As we consider this comparison a validity test for the underlying-field extrapolation, it would be desirable to derive the loop shapes independently. Our connectivity method is therefore based only on geometrical principles and combines the orientation of the loop at the ridge point with the cocircularity constraint proposed by Parent and Zucker (1989).

The procedure is performed in three steps, each of which could be considered a module of its own and performs a very specific task. In Section 2 we explain these individual steps in some detail. In Section 3 we apply the scheme to one of the first images observed by the SECCHI instruments onboard the recently launched STEREO spacecraft (Howard *et al.*, 2007) to demonstrate the capability of our tool. Our procedure offers alternative subschemes and adaptive parameters to be adjusted to the contrast and noise level of the image under consideration. We discuss how the result depends on the choice of some of these parameters. In Section 4 we discuss potential applications of our tool.

2. Method

Our approach consists of three modular steps, each of which is described in one of the following subsections. The first is to find points that presumably are located on the loop axis. At these positions, we also estimate the orientation of the loop for these estimates.

Each item with this set of information is called a ridgel. The next step is to establish probable neighborhood relations between them, which yields chains of ridgels. Finally, each chain is fitted by a smoothing spline, which approximates the loop that gave rise to the ridgels.

2.1. Ridgel Location and Orientation

In terms of image intensities, loop structures are elongated ridge-like intensity maxima. To discriminate the maxima, we need information about the spatial derivatives of the image intensity. Commonly, these derivatives are strongly affected by image noise. In fact, numerical differentiation of data is an ill-posed problem and calls for proper regularization.

We denote by $\mathbf{i} \in \mathbb{I}^2$ the integer coordinate values of the pixel centers in the image and by $\mathbf{x} \in \mathbb{R}^2$ the 2D continuous image coordinates with $\mathbf{x} = \mathbf{i}$ at the pixel centers. We further assume that the observed image intensity $I(\mathbf{i})$ varies sufficiently smoothly so that a Taylor expansion at the cell centers is a good approximation to the true intensity variation $I(\mathbf{x})$ in the neighborhood of $\mathbf{i}$, that is,

$$I(\mathbf{x}) \simeq \tilde{I}(\mathbf{x}) = c + \mathbf{g}^\mathrm{T}(\mathbf{x} - \mathbf{i}) + (\mathbf{x} - \mathbf{i})^\mathrm{T}\mathbf{H}(\mathbf{x} - \mathbf{i}). \tag{1}$$

Pixels close to a ridge in the image intensity can then be detected on the basis of the local derivatives $\mathbf{g}$ and $\mathbf{H}$ (the factor $1/2$ gets absorbed in $\mathbf{H}$). We achieve this by diagonalizing $\mathbf{H}$; that is, we determine the unitary matrix $\mathbf{U}$ with

$$\mathbf{U}^\mathrm{T}\mathbf{H}\mathbf{U} = \mathrm{diag}(h_\perp, h_\parallel), \quad \text{where } \mathbf{U} = (\mathbf{u}_\perp, \mathbf{u}_\parallel), \tag{2}$$

where we assume that the eigenvector columns $\mathbf{u}_\perp$ and $\mathbf{u}_\parallel$ of $\mathbf{U}$ associated with the eigenvalues $h_\perp$ and $h_\parallel$, respectively, are ordered so that $h_\perp \leq h_\parallel$.

We have implemented two ways to estimate the Taylor coefficients. The first is a local fit of Equation (1) to the image within a $(2m + 1) \times (2m + 1)$ pixel box centered around each pixel $\mathbf{i}$:

$$(c, \mathbf{g}, \mathbf{H})(\mathbf{i}) = \operatorname*{argmin} \sum_{\mathbf{j}-\mathbf{i}\in[-m,m]\times[-m,m]} w(\mathbf{i} - \mathbf{j})\big(\tilde{I}(\mathbf{j}) - I(\mathbf{j})\big)^2. \tag{3}$$

We use different weight functions w with their support limited to the box size such as triangle, cosine, or cosine^2 tapers.

The second method commonly used is to calculate the Taylor coefficients (1) not from the original but from a filtered image:

$$\bar{I}(\mathbf{x}) = \sum_{\mathbf{j}} w_d(\mathbf{x} - \mathbf{j})I(\mathbf{j}). \tag{4}$$

As window-function w_d we use a normalized Gaussian of width d. The Taylor coefficients can now be explicitly derived by differentiation of $\bar{I}$, which however acts on the window function w_d instead of on the image data. We therefore effectively use a filter kernel for each Taylor coefficient that relates to the respective derivatives of the window function w_d.

One advantage of the latter method over the local fit described here is that the window width d can be chosen from $\mathbb{R}_+$ while the window size for the fit procedure must be an odd integer $2m + 1$. Both of these methods regularize the Taylor coefficient estimate by the finite size of their window function. In fact, the window size could be considered as a regularization parameter.

A common problem of regularized inversions is the proper choice of the regularization parameter. Lindeberg (1998) has devised a scheme for how this parameter can be optimally chosen. Our third method is a slightly modified implementation of his automated scale-selection procedure. The idea is to apply method two here for each pixel repeatedly with increasing scales d and thereby obtain an approximation of the ridge's second derivative eigenvalues $h_\perp$ and $h_\parallel$, each as a function of the scale d.

Since the $h_\perp$ and $h_\parallel$ are the principal second-order derivatives of the image after being filtered with w_d, they depend on the width d of the filter window roughly in the following way. As long as d is much smaller than the intrinsic width of the ridge, $d_\perp = |(\mathbf{u}_\perp^{\mathrm{T}} \nabla)^2 \log I|^{-1/2}$, the value in $h_\perp$ will be a (noisy) estimate of the true principal second derivative $(\mathbf{u}_\perp^{\mathrm{T}} \nabla)^2 I$ of the image, independent of d. Hence, $h_\perp \propto -I_{\max}/d_\perp^2$ for $d^2 \ll d_\perp^2$. To reduce the noise and enhance the significance of the estimate, we would however like to choose d as large as possible. For $d^2 \gg d_\perp^2$, the result obtained for $h_\perp$ will reflect the shape of the window rather than that of the width of the ridge, $h_\perp \propto -\bar{I}_{\max}/d^2 = -I_{\max}d_\perp/d^3$ for $d^2 \gg d_\perp^2$. Roughly, details near $d \approx d_\perp$ depend on the exact shape of the ridge, and we have

$$h_\perp(d) \sim \frac{-d_\perp}{(d_\perp^2 + d^2)^{3/2}}. \tag{5}$$

For each pixel we consider in addition a quality function

$$q(d) = d^\gamma \big(|h_\perp| - |h_\parallel|\big), \quad \gamma \in (0, 3), \tag{6}$$

which will vary as d^γ for small d and decrease asymptotically to zero for $d \gg d_\perp$ as $d^{\gamma-3}$. In between, $q(d)$ will reach a maximum approximately where the window width d matches the local width $d_\perp$ of the ridge (which is smaller than the scale along the ridge). The choice of the right width d has now been replaced by a choice for the exponent γ. The result, however, is much less sensitive to variations in γ than to variations in d. Smaller values of γ shift the maximum of q only slightly to smaller values of d and hence tend to favor more narrow loop structures. Although γ is a constant for the whole image in this automated scale selection scheme, the window width d is chosen individually for every pixel from the respective maximum of the quality-factor q.

In Figure 1 we show as an example a $\lambda = 171$ Å image of active region NOAA 10930 observed by STEREO/SECCHI on 12 December 2006 at 20:43 UT and the corresponding image of q obtained with $\gamma = 0.75$ and window sizes d in the range of 0.6 to 4 pixels. Clearly, the q factor has a maximum in the vicinity of the loops. The distribution of the scales d for which the maximum q was found for each pixel is shown in Figure 2. About 1/3 of the pixels had optimal widths < one pixel, many of which originate from local elongated noise and moss features of the image. The EUV moss is an amorphous emission that originates in the upper transition region (Berger *et al.*, 1999) and is not associated with loops. For proper loop structures, the optimum width found was about 1.5 pixels with, however, a widely spread distribution.

In the case that $\mathbf{i}$ is located exactly on a ridge, $\mathbf{u}_\perp$ is the direction across and $\mathbf{u}_\parallel$ the direction along the ridge, and $h_\perp$ and $h_\parallel$ are the associated second derivatives of the image intensity in the respective direction. A positive ridge is identified from the Taylor coefficients by means of the following conditions (Lindeberg, 1998):

$$\mathbf{u}_\perp^{\mathrm{T}} \nabla I = \mathbf{u}_\perp^{\mathrm{T}} \mathbf{g} = 0 \quad \text{(a vanishing gradient across the ridge)}, \tag{7}$$

$$\big(\mathbf{u}_\perp^{\mathrm{T}} \nabla\big)^2 I = h_\perp < 0 \quad \text{(a negative second-order derivative across the ridge)}, \tag{8}$$
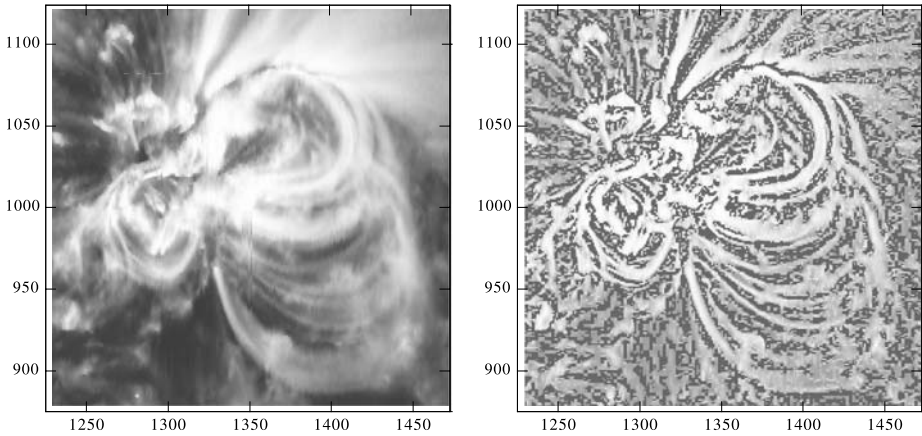
Figure 1 Original image of active region NOAA 10930 observed by STEREO/SECCHI (left) and the corresponding image of the quality factor q (6) obtained from the third ridgel determination method by automated scale selection (right). This image was taken at $\lambda = 171$ Å on 12 December 2006 at 20:43 UT and was not processed by the SECCHI_prep routine.

Figure 2 Distribution of widths d of the window function w_d for which Equation (6) was found to reach a maximum when applied to the data in Figure 1. The maximum was independently determined for each image pixel for which $h_\perp < |h_\parallel|$.
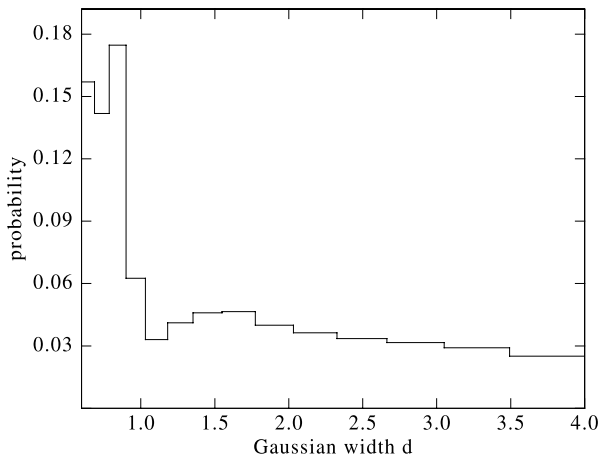
$$\left|\left(\mathbf{u}_\perp^{\mathrm{T}} \nabla\right)^2 I\right| > \left|\left(\mathbf{u}_\parallel^{\mathrm{T}} \nabla\right)^2 I\right| \quad \text{(a second-order derivative magnitude}$$

$$\text{or} \quad |h_\perp| > |h_\parallel| \qquad \text{across the ridge larger than along).} \tag{9}$$

The latter two inequalities are assumed to also hold in the near neighborhood of the ridge and are used to indicate whether the pixel center is close to a ridge.

In the vicinity of the ridge, along a line $\mathbf{x} = \mathbf{i} + \mathbf{u}_\perp t$, the image intensity (1) then varies as

$$I(t) \simeq c + \mathbf{u}_\perp^{\mathrm{T}} \mathbf{g} t + \mathbf{u}_\perp^{\mathrm{T}} \mathbf{u}_\perp h_\perp t^2. \tag{10}$$

According to the first ridge criterion (7), the precise ridge position is where $I(t)$ has its maximum. Hence the distance to the ridge is

$$t_{\max} = -\frac{\mathbf{u}_\perp^{\mathrm{T}} \mathbf{g}}{2 h_\perp \mathbf{u}_\perp^{\mathrm{T}} \mathbf{u}_\perp} \tag{11}$$

and a tangent section to the actual ridge curve closest to $\mathbf{i}$ is

$$\mathbf{r}(s) = \mathbf{i} - \frac{\mathbf{u}_\perp \mathbf{u}_\perp^{\mathrm{T}} \mathbf{g}}{2h_\perp \mathbf{u}_\perp^{\mathrm{T}} \mathbf{u}_\perp} + s\mathbf{u}_\parallel \quad \text{for } s \in \mathbb{R}. \tag{12}$$

Note that $\mathbf{u}_\perp^{\mathrm{T}} \mathbf{u}_\perp = 1$ for a unitary $\mathbf{U}$.

We have implemented two methods for the interpolation of the ridge position from the Taylor coefficients calculated at the pixel centers. One is the interpolation of the ridge center with the help of Equation (12). The second method interpolates the zeros of $\mathbf{u}_\perp^{\mathrm{T}} \mathbf{g}$ in between neighboring pixel centers $\mathbf{i}$ and $\mathbf{j}$ if its sign changes. Hence the alternative realization of condition (7) is

$$\text{if} \quad |c| = \left| \mathbf{u}_\perp^{\mathrm{T}}(\mathbf{i}) \mathbf{u}_\perp(\mathbf{j}) \right| > c_{\min}$$

$$\text{and} \quad \text{sign}(c) \left(\mathbf{u}_\perp^{\mathrm{T}} \mathbf{g} \right)(\mathbf{j}) \left(\mathbf{u}_\perp^{\mathrm{T}} \mathbf{g} \right)(\mathbf{i}) < 0 \quad \text{then}$$

$$\mathbf{r} = \mathbf{i} + t(\mathbf{j} - \mathbf{i}), \tag{13}$$

where

$$t = \frac{(\mathbf{g}^{\mathrm{T}} \mathbf{u}_\perp)(\mathbf{i})}{(\mathbf{g}^{\mathrm{T}} \mathbf{u}_\perp)(\mathbf{i}) - \text{sign}(c)(\mathbf{g}^{\mathrm{T}} \mathbf{u}_\perp)(\mathbf{j})}.$$

The first condition ensures that $\mathbf{u}_\perp(\mathbf{i})$ and $\mathbf{u}_\perp(\mathbf{j})$ are sufficiently parallel or antiparallel. Note that the orientation of $\mathbf{u}_\perp$ of neighboring pixels may be parallel or antiparallel because an eigenvector $\mathbf{u}_\perp$ has no uniquely defined sign.

In general, the interpolation according to Equation (12) yields fewer ridge points along a loop but they have a fairly constant relative distance. With the second method (13), the ridge points can only be found at the intersections of the ridge with the grid lines connecting the pixel centers. For ridges directed obliquely to the grid, the distances between neighboring ridge points produced may vary by some amount. Another disadvantage of the second method is that it cannot detect faint ridges that are just about one pixel wide. It needs at least two detected neighboring pixels in the direction across the ridge to properly interpolate the precise ridge position. The advantage of the second method is that it does not make use of the second-order derivative $h_\perp$, which unavoidably is more noisy than the first-order derivative $\mathbf{g}$. In Figure 3 we compare the ridgels obtained with the two interpolation methods for the same image.

The final implementation of identifying ridge points in the image comprises two steps: first the Taylor coefficients (1) are determined for every pixel and saved for those pixels that have an intensity above a threshold value $I_{\min}$, for which the ridge shape factor $(h_\perp^2 - h_\parallel^2)/(h_\perp^2 + h_\parallel^2)$ exceeds a threshold $s_{\min}$ in accordance with condition (9) and that also satisfy condition (8). The second step is then to interpolate the precise subpixel ridge point position from the derivatives at these pixel centers by either of the two methods. This interpolation complies with the third ridge criterion (7). The ridgel orientations $\mathbf{u}_\perp$ are also interpolated from the cell centers to the ridgel position. The information retained for every ridge point n in the end consists of its location $\mathbf{r}_n$ and the ridge normal orientation $\mathbf{u}_{\perp,n}$ defined modulo π.

2.2. Ridgel Connection to Chains

The connection algorithm we apply to the ridgels to form chains of ridgels is based on the cocircularity condition of Parent and Zucker (1989).
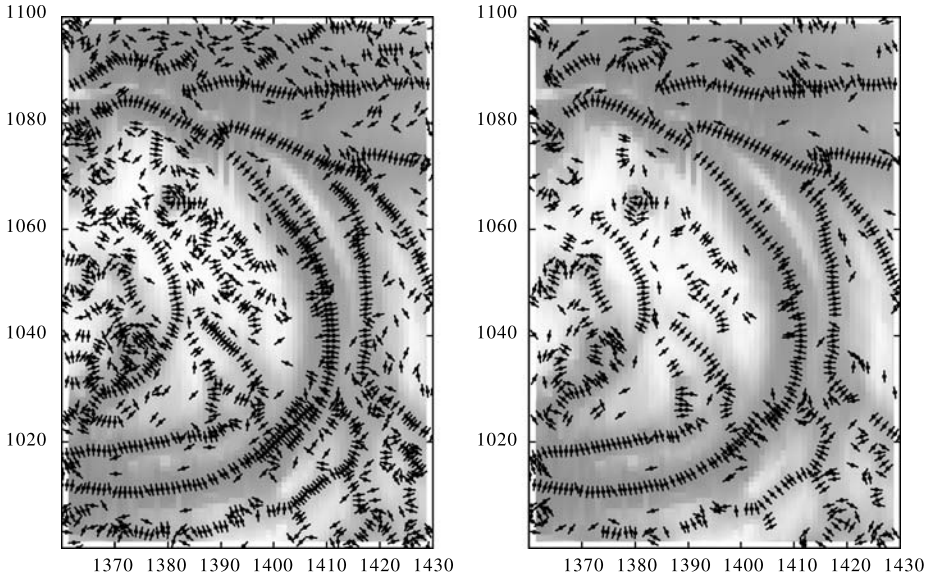
Figure 3 Comparison of the resulting ridgels from interpolation method (12, left) and (13, right). The images show an enlarged portion of the original data in Figure 1. The short sticks denote the local orientation of $\mathbf{u}_\perp$ on the loop trace.

Figure 4 Illustration of angles and distances of a connection element between two ridgels according to the cocircularity condition of Parent and Zucker (1989). The ridgel positions are indicated by small dots; the ridge normal orientation is shown by the line centered at the ridgel position. The axis units are image pixels.
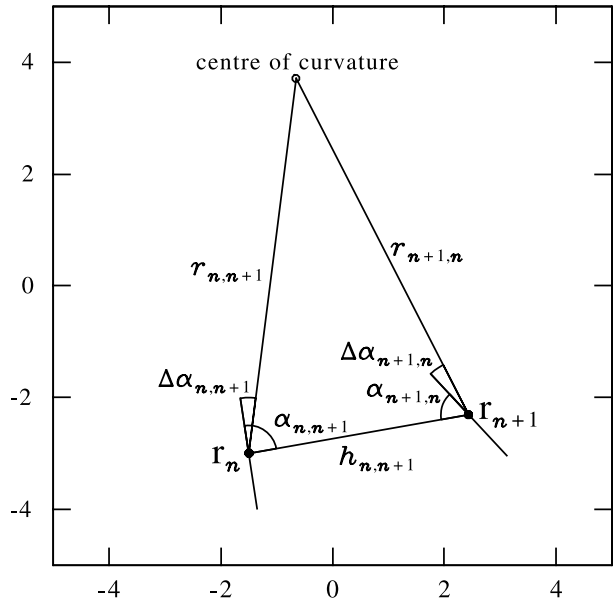
For two ridgels at $\mathbf{r}_n$ and $\mathbf{r}_{n+1}$ a virtual center of curvature can be defined that forms an isosceles triangle with the ridgels as shown in Figure 4. One edge is formed by the connection between the two ridgels of mutual distance $h_{n,n+1}$. The two other triangle edges in this construction connect one of the two ridgels with the center of curvature, which is

chosen so that these two symmetric edges of the isosceles triangle make angles $\Delta\alpha_{n,n+1}$ and $\Delta\alpha_{n+1,n}$ as small as possible with the respective ridgel orientation $\mathbf{u}_{\perp,n}$ and $\mathbf{u}_{\perp,n+1}$, respectively. It can be shown that

$$\min\left(\Delta\alpha_{n,n+1}^2 + \Delta\alpha_{n+1,n}^2\right) \tag{14}$$

requires equal magnitudes for the angles $\Delta\alpha_{n,n+1}$ and $\Delta\alpha_{n+1,n}$. The distance $r_{n,n+1} = r_{n+1,n}$ is the local radius of curvature and can be calculated from

$$r_{n,n+1} = r_{n+1,n} = \frac{\frac{1}{2}h_{n,n+1}}{\cos(\frac{1}{2}(\alpha_{n,n+1} + \alpha_{n+1,n}))}, \tag{15}$$

where $\alpha_{n,n+1}$ is the angle between $\mathbf{r}_{n+1} - \mathbf{r}_n$ and $\pm\mathbf{u}_{\perp,n}$, with the sign being chosen so that $|\alpha_{n,n+1}| < \pi/2$.

With each connection between a pair of ridgels we associate a binding energy that depends on the three parameters just derived in the form

$$e_{n,n+1} = \left(\frac{\Delta\alpha_{n,n+1}}{\alpha_{\max}}\right)^2 + \left(\frac{r_{\min}}{r_{n,n+1}}\right)^2 + \left(\frac{h_{n,n+1}}{h_{\max}}\right)^2 - 3. \tag{16}$$

Note that $\Delta\alpha_{n,n+1}^2 = \Delta\alpha_{n+1,n}^2$ according to the cocircularity construction and hence $e_{n,n+1}$ is symmetric in its indices. The three terms measure three different types of distortions and can be looked upon as the energy of an elastic line element. The first term measures the deviation of the ridgel orientation from strict cocircularity, the second the bending of the line element, and the third term its stretching. The constants $\alpha_{\max}$, $r_{\min}$, and $h_{\max}$ give us control on the relative weight of the three terms. If we only accept connections with a negative value for the energy (16), then $r_{\min}$ is the smallest acceptable radius of curvature and $h_{\max}$ is the largest acceptable distance.

In practical applications, the energy (16) is problematic since it puts nearby ridgel pairs with small distances $h_{n,n+1}$ at a severe disadvantage because small changes of their $\mathbf{u}_{\perp}$ easily reduces the radius of curvature $r_{n,n+1}$ below acceptable values. We therefore allow for measurement errors in $\mathbf{r}$ and $\mathbf{u}_{\perp}$ and the final energy considered is the minimum of Equation (16) within these given error bounds.

The final goal is to establish a whole set of connections between as many ridgels as possible so that the individual connections add up to chains. Note that each ridgel has two "sides" defined by the two half-spaces that are separated by the ridgel orientation $\mathbf{u}_{\perp}$. We only allow at most one connection per ridgel in each of these "sides." This restriction avoids junctions in the chains that we are going to generate. The sum of the binding energies (16) of all accepted connections ideally should attain a global minimum in the sense that any alternative set of connections that complies with this restriction should yield a larger energy sum.

We use the following approach to find a state that comes close to this global minimum. The energy $e_{n,n+1}$ is calculated for each ridgel pair less than $h_{\max}$ apart, and those connections that have a negative binding energy are stored. These latter are the only connections we expect to contribute to the energy minimum. Next we order the stored connections according to their energy and connect the ridgels to chains starting from the lowest energy connection. Connections to one side of a ridgel that has already been occupied by a lower energy connection before are simply discarded.

2.3. Curve Fits to the Ridgel Chains

In this final section we calculate a smooth fit to the chains of ridgels obtained. The fit curve should level out small errors in the position and orientation of individual ridgels. We found from experiments that higher order spline functions are far too flexible for the curves we aim at. We expect that magnetic-field lines in the corona do not rapidly vary their curvature along their length and we assume this also holds for their projections on EUV images. We found that parametric polynomials of third or fifth degree are sufficient for our purposes. Hence for each chain of ridgels we seek polynomial coefficients $\mathbf{q}_n$ that generate a two-dimensional curve

$$\mathbf{p}(t) = \sum_{n=0}^{5} \mathbf{q}_n t^n \quad \text{for } t \in [-1, 1] \tag{17}$$

that best approximates the chain of ridgels. What we mean by "best approximation" will be defined more precisely in the following. The relevant parameters of this approximation are sketched in Figure 5.

The polynomial coefficients $\mathbf{q}$ of a fit (17) are determined by minimizing

$$\sum_{i \in \text{chain}} \left(\mathbf{d}_i^{\mathrm{T}} \mathbf{d}_i \right) + \mu \left(\mathbf{p}''^{\mathrm{T}} \mathbf{p}'' \right)(t_i), \tag{18}$$

where

$$\mathbf{d}_i = \mathbf{r}_i - \mathbf{p}(t_i)$$

with respect to $\mathbf{q}_n$ for a given μ. Initially, we distribute the curve parameters t_i in the interval $[-1, 1]$ such that the differences $t_i - t_j$ of neighboring ridgels are proportional to the geometric distances $|\mathbf{r}_i - \mathbf{r}_j|$. The $\mathbf{p}''$ are the second-order derivatives of (17). Hence, the

Figure 5 Sketch of the curve-fit parameters. The ridgels are represented by their location and the two-pixel-long bar of the ridgel orientation. For each ridgel i, the proximity to the smooth-fit curve is expressed by its distance d_i and the angle $\Delta\alpha_i$ between the distance direction of $\mathbf{d}_i$ to the curve and the ridgel orientation. Another measure of the quality of the curve is the inverse radius of curvature r.
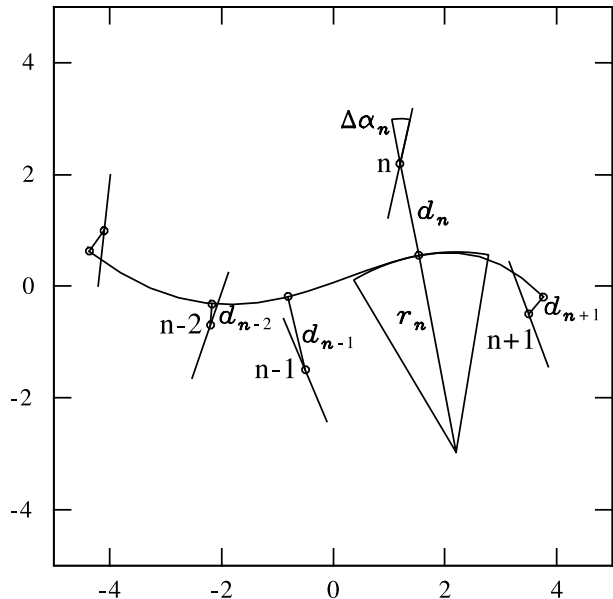
second term increases with increasing curvature of the fit whereas a more strongly curved fit is required to reduce the distances $\mathbf{d}_i$ between $\mathbf{r}_i$ and the first-order closest curve point $\mathbf{p}(t_i)$.

The minimum coefficients $\mathbf{q}_n(\mu)$ can be found analytically in a straightforward way. Whenever a new set of $\mathbf{q}_n(\mu)$ has been calculated, the curve nodes t_i are readjusted by

$$t_i = \operatorname{argmin}_t \big(\mathbf{r}_i - \mathbf{p}(t)\big)^2, \tag{19}$$

so that $\mathbf{p}(t_i)$ is always the point along the curve closest to the ridgel.

For different μ, this minimum yields fit curves with different levels of curvature. The local inverse radius of curvature can at any point along the curve be calculated from Equation (17) by

$$\frac{1}{r(t)} = \frac{|\mathbf{p}''(t) \times \mathbf{p}'(t)|}{|\mathbf{p}'(t)|^3}. \tag{20}$$

The final μ is then chosen so that

$$E_{\text{chain}}(\mu) = \sum_{i \in \text{chain}} \frac{d_i^2}{d_{\max}^2} + \sum_{i \in \text{chain}} \frac{\Delta\alpha_i^2}{\alpha_{\max}^2} + r_{\min}^2 \int_{-1}^{1} \frac{1}{r(t)^2}\, \mathrm{d}t \tag{21}$$

is a minimum where $\Delta\alpha_n$ is the angle between the local normal direction of $\mathbf{d}_n$ of the fit curve and the ridgel orientation $\pm\mathbf{u}_{\perp,n}$, with the sign again chosen to yield the smallest possible $|\Delta\alpha_i|$. The meaning of the terms is obvious, and clearly the first two terms in general require a large curvature, which is limited by the minimization of the last term.

Expression (21) depends nonlinearly on the parameter μ, which we use to control the overall curvature. The minimum for Equation (21) is found by iterating μ starting from a large numerical value (*i.e.*, a straight-line fit). The parameters $r_{\min}$, $\alpha_{\max}$, and $d_{\max}$ can be used to obtain fits with a different balance between the mean square spatial and angular deviation of the fit from the "observed" chain of ridgels and the curvature of the fit. Unless these parameters are chosen reasonably (*e.g.* $r_{\min}$ not too small), we have always found a minimum for Equation (21) after a few iteration steps.

In the left part of Figure 6 we show the final fits obtained. For this result, the ridgels were found by automated scaling and interpolated by method (12), the parameters in Equa-
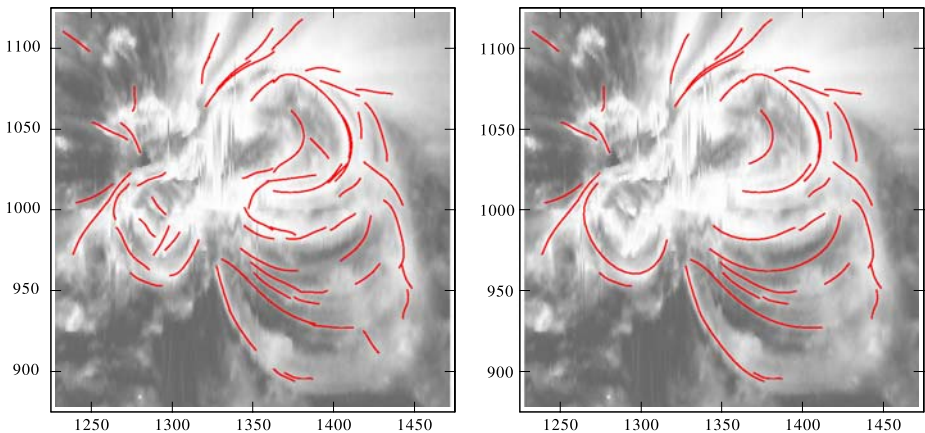
Figure 6 Fit curves obtained for those chains that involve ten or more ridgels (left) and curves remaining after cleaning of those curves resulting from moss (right).

tions (16) and (21) were $h_{max} = 3.0$ pixels, $r_{min} = 15.0$ pixels, and $a_{max} = 10.0$ degrees. The fits are represented by fifth-degree parametric polynomials.

Obviously, the image processing cannot easily distinguish between structures resulting from moss and bright surface features and coronal loops. Even the observer is sometimes misled and there are no rigorous criteria for this distinction. Roughly, coronal loops produce longer and smoother fit curves, but there is no strict threshold because it may appear that the fit curve is split along a loop where the loop signal becomes faint. As a rule of thumb, a restriction to smaller curvature by choosing a higher parameter r_{max} and discarding shorter fit curves tends to favor coronal loops. Eventually, however, loops are suppressed, too. We have therefore appended a user interactive tool as the last step of our processing to allow us to eliminate unwanted curves and merge or split curves when smooth fits result with an energy (21) of the output fits not much higher than the energy of the input. The left part of Figure 6 shows the result of such a cleaning step.

3. Application

In this section we present an application of our segmentation tool to another EUV image of active region NOAA 10930 taken by the SECCHI instrument onboard STEREO A. This EUV image was observed at $\lambda = 195$ Å on 12 December 2006 at 23:43:11 UT. At that time the STEREO spacecraft were still close together so stereoscopy could not be applied. We therefore selected an image that was taken close to the MDI magnetogram observed at 23:43:30 UT on the same day. It is therefore possible to calculate magnetic-field lines from an extrapolation model and project them onto the STEREO view direction to compare them with the loop fits obtained with our tool. In Figure 7 the MDI contour lines of the line-of-sight field intensity were superposed on the EUV image.
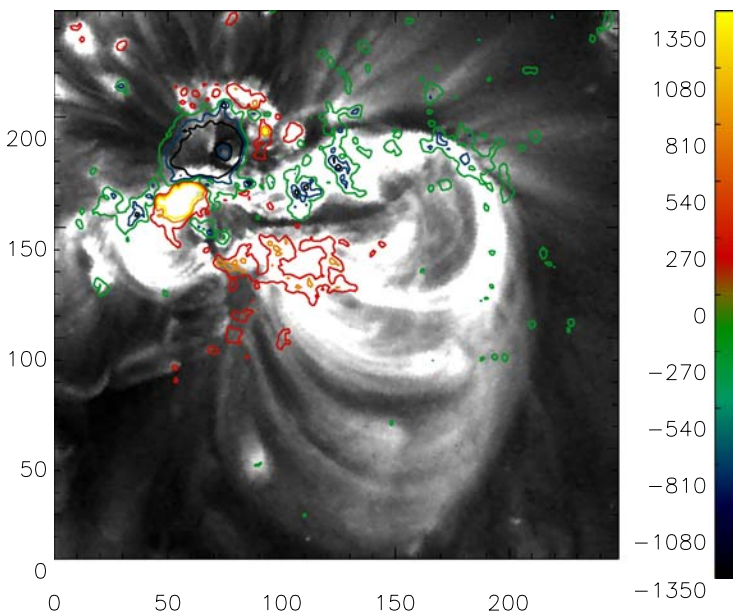
Figure 7 MDI contours overlaid on the STEREO/SECCHI EUV image for NOAA 10930. The EUV and MDI data were recorded on 12 December 2006 at 23:43:11 UT and 23:43:30 UT, respectively. The color code on the right indicates the field strength at the contour lines in gauss.
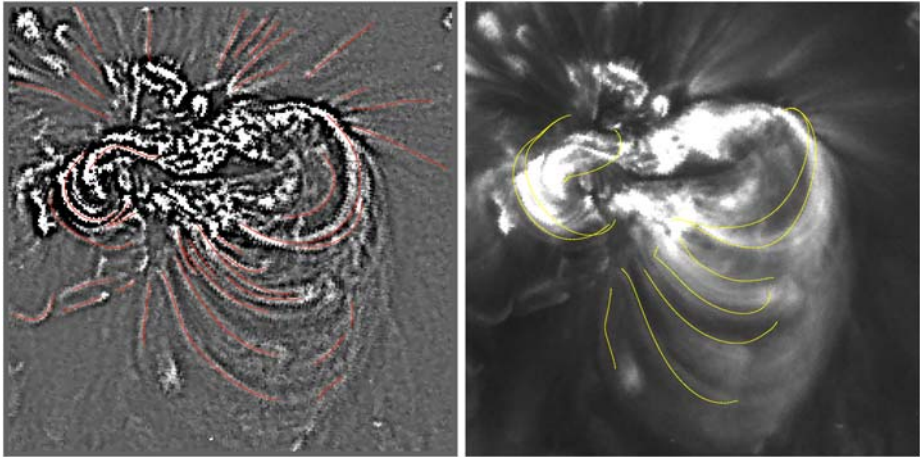
Figure 8 The left diagram shows as red lines the loops identified by the segmentation tool for the EUV image in Figure 7. To show the loops more clearly, the image in the background was contrast enhanced by an unsharp mask filter. The right diagram displays in yellow field lines calculated from the MDI data. The field lines were selected so that they are located closest to the extracted loops in the left part of the image. See the text for more details on how the field lines were determined.

The loop fits here were obtained by applying the automated scaling with d up to two pixels (*i.e.* window sizes up to $2d + 1 = 5$ pixels) to identify the ridgels. Pixels with maximum quality q below 0.4 were discarded and we applied method (12) to interpolate the local ridge maxima. $h_{max} = 5.0$ pixels, $r_{min} = 15.0$ pixels, and $a_{max} = 10.0°$. The fits are fifth-degree parametric polynomials. In Figure 8, we show some of the fits obtained that are most likely associated with a coronal loop. They are superposed onto the EUV image as red lines. Those loops that were found close to computed magnetic-field lines are displayed again in the left part of Figure 9 with loop numbers so that they can be identified.

The magnetic-field lines were computed from the MDI data by an extrapolation based on a linear force-free field model (see Seehafer, 1978, and Alissandrakis, 1981, for details). This model is a simplification of the general nonlinear, force-free magnetic-field model:

$$\nabla \times \mathbf{B} = \alpha \mathbf{B}, \quad \text{where } \mathbf{B} \cdot \nabla \alpha = 0, \tag{22}$$

and α may vary on different field lines. An extrapolation of magnetic surface observations based on this model requires boundary data from a vector magnetograph. The linear force-free field model treats α as a global constant. The advantage of the linear force-free field model is that it requires only a line-of-sight magnetogram, such as MDI data, as input.

A test of the validity of the linear force-free assumption is to determine different values of α from a comparison of field lines with individual observed loop structures (*e.g.*, Carcedo *et al.*, 2003). The range of α obtained then indicates how close the magnetic field can be described by the linear model. Since the linear force-free field has the minimum energy for given normal magnetic boundary field and magnetic helicity, a linear force-free field is supposed to be much more stable than the more general nonlinear field configuration (Taylor, 1974).

We calculated about 5000 field lines with the linear force-free model with the α value varied in the range from -0.0427 to 0.0356 Mm^{-1}. These field lines were then projected onto the EUV image for a comparison with the detected loops.
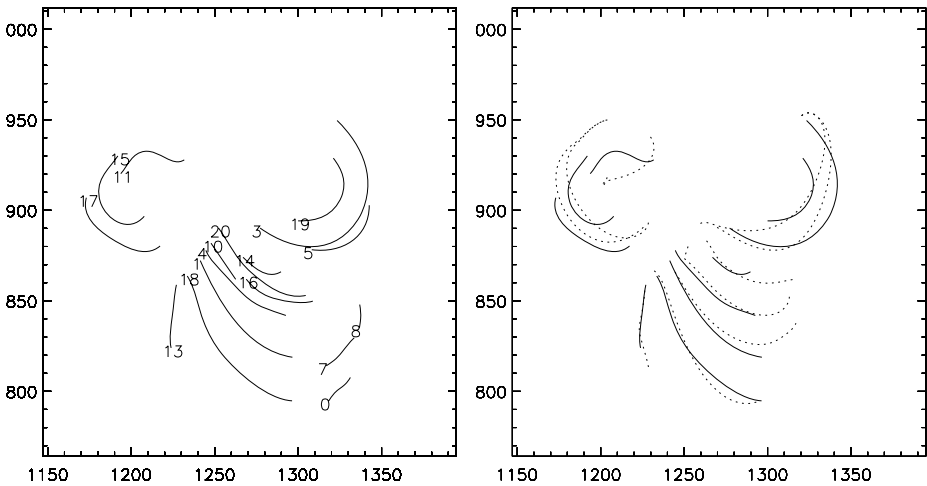
Figure 9 The left panel shows the loops identified by the segmentation tool that corresponds to the closed magnetic filed lines. In the right panel are the loops (solid lines) with their best-fitting field lines (dotted lines). The x and y axes are in units of EUV pixels.

Table 1 Identified loops, the averaged distances in units of pixels between the loop and the best-fitting field line, and α values of the best-fitting field lines.

Loop	$C_l(b)$ (pixel)	α (10^{-3} Mm^{-1})
1	3.1957	−10.680
3	3.7523	−35.600
4	2.3432	−9.2560
11	10.7692	−35.600
13	0.4864	2.1360
14	1.3636	−9.2560
15	4.2386	17.088
17	4.8912	16.376
18	2.4256	−14.240
19	2.5388	−32.752

For each coronal loop l_i, we calculate the average distance of the loop to every projected field line b_j discarding those field lines that do not fully cover the observed loop l_i. This distance is denoted by $C_{l_i}(b_j)$. For details of this distance calculation see Feng *et al.* (2007). In the end we could find a closest field line for every coronal loop by minimizing $C_{l_i}(b_j)$. The detected loops and their closest field lines are plotted in the right diagram of Figure 9. An overplot of the closest field lines onto the EUV image is shown in Figure 8.

In Table 1 we list the distance measure C along with the loop number and the linear force-free parameter α for the closest field line found. We find that our α values are not uniform over this active region; that is, the linear force-free model is not adequate to describe the magnetic properties of this active region. This is also seen by the characteristic deviation at their upper right end in Figure 8 between the eastward-inclined loops (solid) and their closest, projected field lines (dotted). With no value of α the shape of these loops could be satisfactorily fitted. Further evidence for strong and inhomogeneous currents in the active region loops is provided by the fact that only 2.5 hours later, at 02:14 UT on 13 December,

a flare occurred in this active region and involved the magnetic structures associated with loops 2, 4, and 17.

4. Discussion

EUV images display a wealth of structures and there is an important need to reduce this information for specified analyses. For the study of the coronal magnetic field, the extraction of loops from EUV images is a particularly important task. Our tool intends to improve earlier work in this direction. Whether we have achieved this goal can only be decided from a rigorous comparison, which is underway elsewhere (Aschwanden *et al.*, 2007). At least from a methodological point of view, we expect that our tool should yield improved results compared to those of Strous (2002, unpublished) and Lee, Newman, and Gary (2006).

From the EUV image alone it is often difficult to decide which of the features are associated with coronal loops and which are due to moss or other bright surface structures. A final comparison of the loops with the extrapolated magnetic field and its field line shapes is therefore very helpful for this distinction. Yet we have avoided involving the magnetic-field information in the segmentation procedure that extracts the loops from the EUV image because this might bias the loop shapes obtained.

For the case we have investigated, we find a notable variation of the optimal α values and also characteristic deviation of the loop shapes from the calculated field lines. These differences are evidence of the fact that the true coronal magnetic field near this active region is not close to a linear force-free state. This is in agreement with earlier findings. Wiegelmann *et al.* (2005), for example, have shown for another active region that a nonlinear force-free model describes the coronal magnetic field more accurately than linear models. The computation of nonlinear models is, however, more involved because of the nonlinearity of the mathematical equations (*e.g.*, Wiegelmann, 2004; Inhester and Wiegelmann, 2006). Furthermore, these models require photospheric vector magnetograms as input, which were not available for the active region investigated.

Coronal loop systems are often very complex. To access them in three dimensions, the new STEREO/SECCHI telescopes now provide EUV images that can be analyzed with stereoscopic tools. We plan to apply our loop-extraction program to EUV images from different viewpoints and undertake a stereoscopic reconstruction of the true 3D structure of coronal loops along the lines described by Inhester (2006) and Feng *et al.* (2007). Knowledge of the 3D geometry of a loop allows us to estimate more precisely its local EUV emissivity. From this quantity we hope to be able to derive more reliably the plasma parameters along the length of the loop.

Other applications can be envisaged. One interesting application of our tool will be the investigation of loop oscillations. Here, the segmentation tool will be applied to times series of EUV images. We are confident that oscillation modes can be resolved and, in the case of a STEREO/SECCHI pairwise image sequence, the polarization of the loop oscillation can also be discerned.

References

Alissandrakis, C.E.: 1981, *Astron. Astrophys.* **100**, 197.

Aschwanden, M., Lee, J.K., Gary, G.A., Smith, M., Inhester, B.: 2007, *Solar Phys.*, accepted.

Berger, T., De Pontieu, B., Fletcher, L., Schrijver, C., Tarbell, T., Title, A.: 1999, *Solar Phys.* **190**, 409.

Carcedo, L., Brown, D.S., Hood, A.W., Neukirch, T., Wiegelmann, T.: 2003, *Solar Phys.* **218**, 29.

Dimas, A., Scholz, M., Obermayer, K.: 2002, *IEEE Trans. Image Process.* **11**(7), 790.

Feng, L., Wiegelmann, T., Inhester, B., Solanki, S., Gan, W.Q., Ruan, P.: 2007, *Solar Phys.* **241**, 235.

Howard, R., Moses, J., Vourlidas, A., Newmark, J., Socker, D., Plunckett, S., Korendyke, C., Cook, J., Hurley, A., Davila, J., Thompson, W., St. Cyr, O., Mentzell, E., Mehalick, K., Lemen, J., Wuelser, J., Duncan, D., Tarbell, T., Harrison, R., Waltham, N., Lang, J., Davis, C., Eyles, C., Halain, J., Defise, J., Mazy, E., Rochus, P., Mercier, R., Ravet, M., Delmotte, F., Auchère, F., Delaboudinière, J., Bothmer, V., Deutsch, W., Wang, D., Rich, N., Cooper, S., Stephens, V., Maahs, G., Baugh, R., McMullin, D.: 2007, *Space Sci. Rev.*, in press (http://secchi.lmsal.com/EUVI/DOCUMENTS/howard.pdf).

Inhester, B.: 2006, *Int. Space Sci. Inst.*, submitted (astro-ph/0612649).

Inhester, B., Wiegelmann, T.: 2006, *Solar Phys.* **235**, 201.

Jang, J.H., Hong, K.S.: 2002, *Pattern Recognit.* **35**, 807.

Koller, T., Gerig, B., Székely, G., Dettwiler, D.: 1995, In: *Proceedings Fifth Int. Conf. on Computer Vision (ICCV95)*, IEEE Computer Society Press, Washington, 864.

Lee, J.K., Newman, T.S., Gary, G.A.: 2006, *Pattern Recognit.* **39**, 246.

Lindeberg, T.: 1998, *Int. J. Comput. Vis.* **30**(2), 117.

Medioni, G., Tang, C.K., Lee, M.S.: 2000, http://citeseer.ist.psu.edu/medioni00tensor.html.

Nguyen, H., Worring, M., van den Boomgaard, R.: 2000, http://citeseer.ist.psu.edu/article/nguyen00watersnakes.html.

Parent, P., Zucker, S.: 1989, *IEEE Trans. Pattern Anal. Mach. Intell.* **11**, 823.

Seehafer, N.: 1978, *Solar Phys.* **58**, 215.

Starck, J.L., Donoho, D.L., Candès, E.J.: 2003, *Astron. Astrophys.* **398**, 785.

Steger, C.: 1998, *IEEE Trans. Pattern Anal. Mach. Intell.* **20**(2), 113.

Taylor, J.B.: 1974, *Phys. Rev. Lett.* **33**, 1139.

Wiegelmann, T.: 2004, *Solar Phys.* **219**, 87.

Wiegelmann, T., Lagg, A., Solanki, S.K., Inhester, B., Woch, J.: 2005, *Astron. Astrophys.* **433**, 701.

Zhang, Q., Yan, H.: 2004, *Pattern Recognit.* **37**, 2233.